Rotation Analysis of a Microfabricated Fatigue Test Structure

by

Michael J. Gordon

Submitted to the Department of Electrical Engineering and Computer Science
in partial fulfillment of the requirements for the degree of

Master of Science in Electrical Engineering and Computer Science

at the

MASSACHUSETTS INSTITUTE OF TECHNOLOGY

January 1999
[February, 1999]

Author .....
Department of Electrical Engineering and Computer Science
January 29, 1999

Certified by .....
Dennis M. Freeman
Associate Professor of Electrical Engineering
Thesis Supervisor

Accepted by .....
Arthur C. Smith
Chairman, Department Committee on Graduate Students

Rotation Analysis of a Microfabricated Fatigue Test Structure

by

Michael J. Gordon

Submitted to the Department of Electrical Engineering and Computer Science
on January 29, 1999, in partial fulfillment of the
requirements for the degree of
Master of Science in Electrical Engineering and Computer Science

Abstract

Tools for motion analysis of microelectromechanical systems (MEMS) are primitive by comparision to those available for electrical analysis of microfabricated electronic circuits. We have developed a method called computer microvision to measure motions of MEMS with nanometer precision. Computer microvision analyzes images from a light microscope with machine vision algorithms. In this thesis, we develop a new method for accurately measuring in-plane rotations of a microfabricated fatigue test structure using computer microvision. In the fatigue test structure, provided by Exponent Failure Analysis Associates, Inc., a proof mass is rotated about its single point of attachment to the substrate. Motions are induced by applying an electrical stimulus to a comb drive. In-plane rotation was measured to an accuracy of 10 millidegrees, or about 36 arc seconds, over a range of ± 1 degree. This method for measuring rotation generalizes to other rotating structures as well.

Thesis Supervisor: Dennis M. Freeman
Title: Associate Professor of Electrical Engineering

Acknowledgments

First, I want to thank my advisor, Dennis Freeman. He's been a fountain of knowledge on all topics. Also, he's been essential in figuring out the direction of my thesis—even if it has changed dramatically over the past six months. Thank you for the hours of rigorous editing and help with my writing.

I also want to thank A.J. Aranyosi, my officemate, for helping me with countless computer problems and for proofreading my thesis. Michael "Merm" Mermelstein gave me excellent advice and helped me with numerous technical problems—thanks. Samson Timoner, thank you for editing my thesis with an extremely fine tooth comb. I would never have collected my data if not for the help of Stanley Hong. Thanks to the Micromechanics Lab secretary, Janice Balzer, for always coming through with our "extremely urgent" orders.

Finally, I want to thank my girlfriend, Elizabeth Potts, for her support and help in improving my writing. Thanks for tolerating my stress over the past few months. Thanks also to my parents, Pat and Carl Gordon, for their support.

Contents

List of Figures

List of Tables

Chapter 1

Introduction

Microelectromechanical systems (MEMS) are machines with dimensions ranging from a few micrometers to a few millimeters. They have many applications, including accelerometers for vehicle crash detection, pressure sensors used in engines and medical devices, gyroscopes in vehicle attitude control systems, chemical sensors for detecting combustible gases, micro-mirrors for projection displays, and many others. MEMS are fabricated using methods that are similar to those used to manufacture microelectronic chips.

Powerful tools exist to make in situ electrical measurements of microfabricated electronic circuits; however, few tools exist for testing the motions of MEMS. This is a serious problem for MEMS designers and manufacturers since the lack of micromechanical measurement tools can result in a large number of costly prototype designs or defects in a product going unnoticed until after packaging and possibly shipment. The commercialization and demand for MEMS has exploded in the last decade creating a crucial need for new analysis tools.

Our group designed a system called computer microvision to measure and analyze the motions of MEMS (Freeman and Davis, 1996; Freeman et al., 1998). Computer microvision is a method which uses machine vision algorithms to analyze video images taken with light microscopy. This system was first used to measure the motions of biological structures in the ear (Davis, 1994) and later to measure a microfabricated accelerometer (Freeman and Davis, 1996) and a microfabricated gyroscope (John-

son, 1997). These measurements demonstrated computer microvision's potential as a MEMS measurement tool.

We have applied computer microvision to analyze the motion of a polysilicon fatigue test structure (Figure 1-1) designed by Exponent Failure Analysis Associates (Brown et al., 1997) and manufactured by MCNC (formerly Microelectronics Center of North Carolina). The machine consists of a shuttle (Figure 1-1) suspended above the substrate by a narrow beam with a v-shaped notch. The device tests the durability and failure strength of polysilicon by bending the shuttle around the notched pivot point (Figure 1-1). By placing voltage across a "comb drive," electrostatic forces drive the shuttle so that it oscillates in the plane of the structure around the pivot point at the shuttle's mechanical resonant frequency ($\sim$ 40 kHz). The bending concentrates stress at the trough of the pivot point and eventually causes the beam to fracture.

This thesis develops a robust method for accurately and precisely measuring rotations of the fatigue test structure. Two techniques are developed. Both use translation estimates at many points on an image to estimate rotation. The first uses translations at a pair of points and then averages rotation estimates from many pairs. The second uses a weighted least squares approach, which proved more reliable and robust. We achieved an accuracy of 10 millidegrees (36 arc seconds) over a range of ± 1 degree.

While only in-plane rotation (yaw, as in airplane terminology) is measured in this thesis, the method can also be extended to measure two out-of-plane angles (pitch and roll). The fatigue test structure was used to develop the measurement method, but the technique is applicable to other MEMS devices and larger rotating objects.

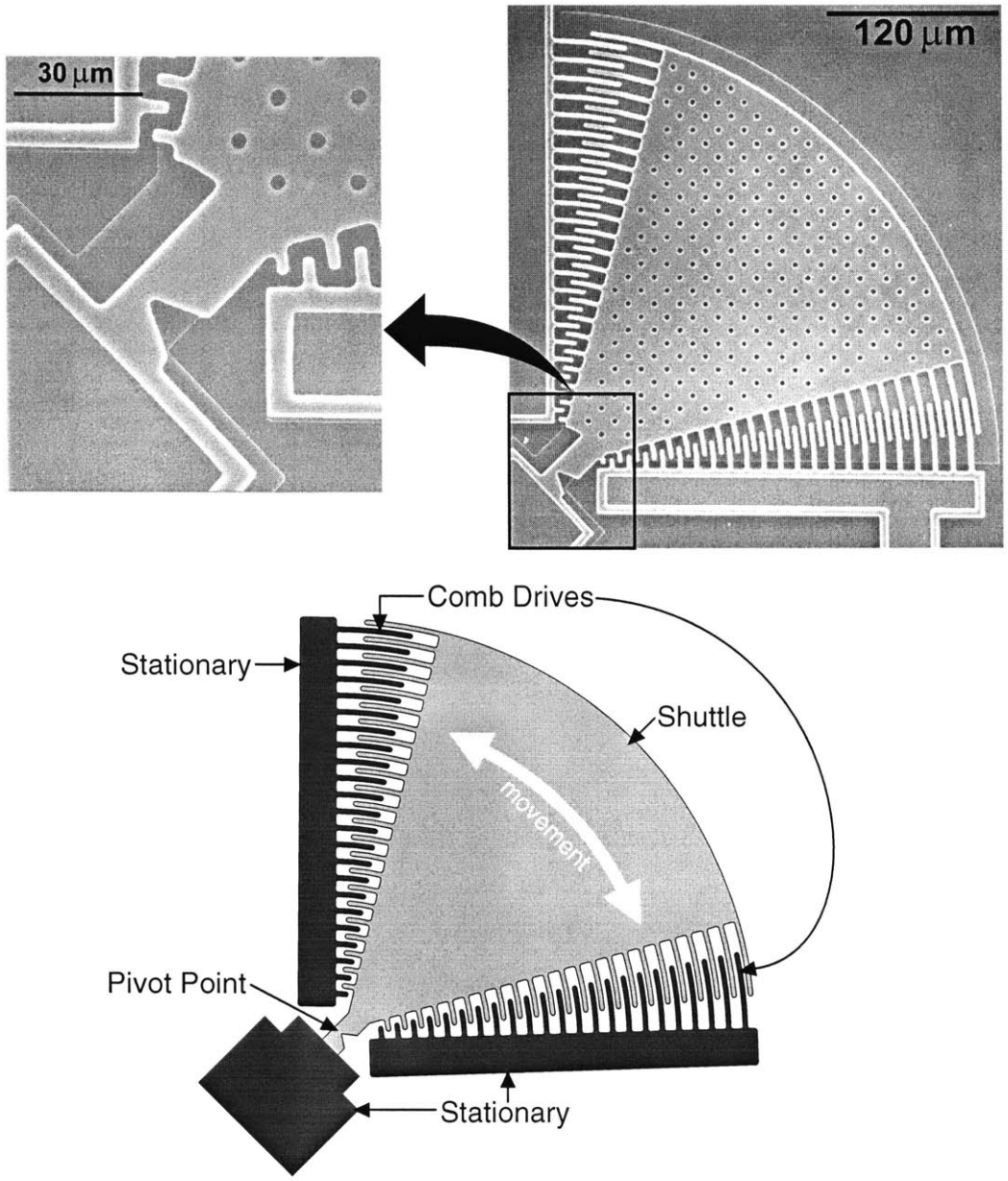

Figure 1-1: Microfabricated fatigue test structure. The images (top right and left) are a scanning electron micrographs (SEM) of a fatigue test structure (courtesy of Exponent Failure Analysis). The schematic (bottom) shows a shuttle which is suspended above the substrate by a narrow beam containing a v-notched pivot point. The pivot point is shown in detail in the zoom-in picture (top left). The dark shaded regions (bottom) are fixed to the substrate. The bending concentrates stress at the trough of the pivot point and eventually causes the beam to fracture.

Chapter 2

Data Acquisition

Motion analysis of a MEMS device involves two steps: data acquisition and data analysis. Data acquisition involves driving the device and collecting a series of images as it moves. Data analysis uses robot vision algorithms to estimate motion from the images. In this chapter we discuss data acquisition leaving the data analysis for Chapter 3.

A light microscope and camera images the fatigue test structure while an electrical signal drives the device (Figure 2-1). An LED strobed once per stimulus period at a chosen phase (Figure 2-1), gives a snapshot of the device's position at the specified phase. The process is repeated at several stimulus phases. Machine vision algorithms are used to estimate the change in position of the device between sucessive images. From these estimates, the periodic motion of the device is determined.

2.1 Fatigue test structure setup

The fatigue test structure, designed by Exponent Failure Analysis (Brown et al., 1997), is built out of polysilicon and lies on a 4 by 4 mm die (square piece of silicon). The die is mounted in a 48 pin dual inline package (DIP). The DIP is mounted in a socket attached to the stage of a light microscope.

To drive the fatigue test structure, the shuttle is grounded (lower left of Figure 2-2) and a 120 V peak-to-peak 20 kHz sine wave with no DC offset is applied to the

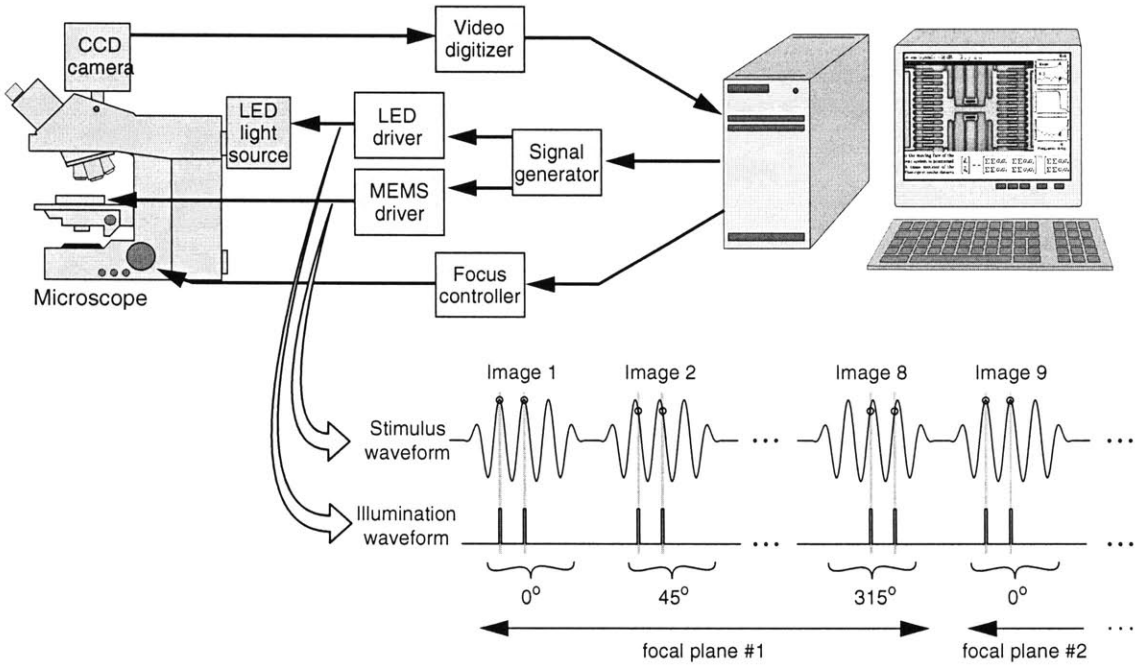

Figure 2-1: Computer microvision measurement system. The test device is placed on the stage of the microscope (left). A computer controls a signal generator that provides two synchronized waveforms: one to the MEMS driver to drive motions of the test device and one to the LED driver to strobe the LED light source. Shown at bottom are typical waveforms. A sinusoidal stimulus drives the motions. The first image is acquired with the CCD camera when light from the LED (illumination waveform) samples the image at times corresponding to peaks in the stimulus waveform. Successive images are acquired at different phases. (Figure adapted from Freeman, et al., 1998)

"bottom" comb drive. Since mechanical force on the shuttle is proportional to the square of the applied voltage ($F \propto V^2$) (Senturia and Schmidt, 1997), the shuttle oscillates at 40 kHz, twice the frequency of the stimulus voltage ($f_{force} = 2f_{voltage}$). The mechanical force rotates the shuttle around the pivot point.

2.2 Video microscopy

The fatigue test structure is mounted on the stage of a microscope (Zeiss Axioplan 2 Motorized Research Microscope, Oberkochen, Germany), resting on a vibration

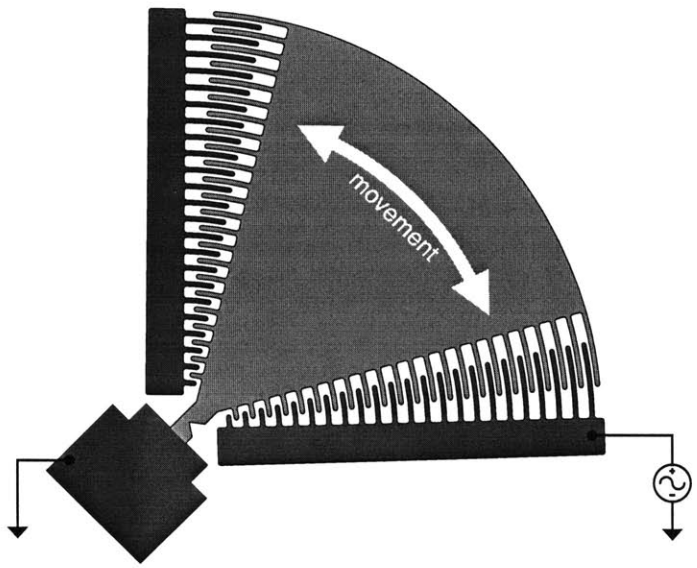

Figure 2-2: Stimulus condition used in analyzing the fatigue test structure. To drive the fatigue test structure, the shuttle is connected to ground, and the lower comb drive is connected to the voltage source. The shuttle rotates in the direction indicated by the white arrow.

isolation table (Integrated Dynamics Engineering, Woburn, MA). The microscope objective is a Zeiss LD-Epiplan 20× with a numerical aperature of 0.4 and a working distance of 9.8 mm. The microscope projects a magnified image of the device onto a scientific grade, 10-bit CCD camera (Kodak Megaplus 1.6i) which has 1534 × 1024 pixels with 9 μm spacing.

2.3 Stroboscopic illumination

Since the fastest scientific-grade CCD camera can acquire images on the order of tens of Hertz, we use stroboscopic illumination to image faster motions (currently up to 100 kHz). We use a green LED as the light source (Nichia NSPG500S, Tokushima 774, Japan) because LEDs are faster than most other light sources and because the microscope optics are optimized for green light. Our technique of stroboscopic illumination is illustrated in the waveforms of Figure 2-1 where light from the LED illuminates the target at a specified phase of motion. The LED's shortest light pulse is roughly 1 μs and is limited by the speed of our drive electronics. A halogen lamp housing with the halogen lamp removed collects the LED's light. The plastic lens originally covering the LED's die is milled away and the flat surface is polished (Figure 2-3), so that illumination is Köhler (Inoué, 1986).

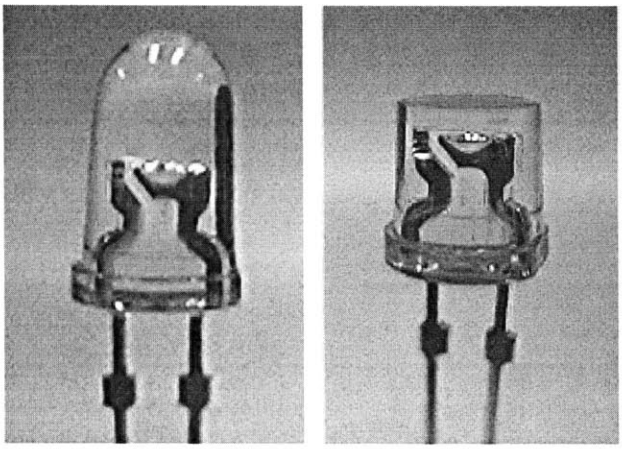

(a) (b)

Figure 2-3: Regular and flat top LED. (a) A standard Nichia green LED. The plastic lens on top of the die is not suitable for Köhler illumination. (b) The plastic lens that originally covered the LED's die was milled away and the flat surface was polished, so that illumination is Köhler (Inoué, 1986)

2.4 Motion estimates from video images

Displacements between images are estimated using motion detection algorithms described elsewhere (Davis and Freeman, 1998a; Davis and Freeman, 1998b; Karu, 1997). Motion as small as two nanometers can be reliably measured between two images even though image resolution is roughly limited to the wavelength of light (550 nm for the green LED). Sinusoidal motions are characterized by acquiring 16 images using stroboscopic illumination at evenly-spaced phases of the stimulus waveform. The LED is turned on for $\frac{1}{16}$ of the stimulus period.

Chapter 3

Measuring Rotation: Pairs of ROIs

The major goal of this thesis is to develop a method to measure rotation accurately and robustly from video images. We previously developed analysis tools to measure tranlational motions from video images using a gradient method adopted from machine vision (Davis and Freeman, 1998a). Also, an algorithm for measuring rotation from video images was previously developed using a hierarchical gradient-based approach (Karu, 1997). Unfortunately, Karu's rotation measurement technique has not proven reliable and robust under noisy conditions. However, the translation measurement method has been well used and proven more reliable under noisy conditions than Karu's rotation measurement method. Also, the statistical nature of the translation measurement technique is well understood in the presence of noise. These observations have prompted us to develop a new rotation measurement technique built on top of the translation measurement method. We use translation estimates at multiple points on video images of a rigid body to estimate its in-plane rotation.

We briefly discuss previously developed translation motion analysis and then we develop a method for calculating rotation from many translation estimates.

3.1 Translational motion analysis

We measure translation motion from video images using a gradient method (Davis and Freeman, 1998a; Horn and Weldon, Jr., 1988). The technique uses changes

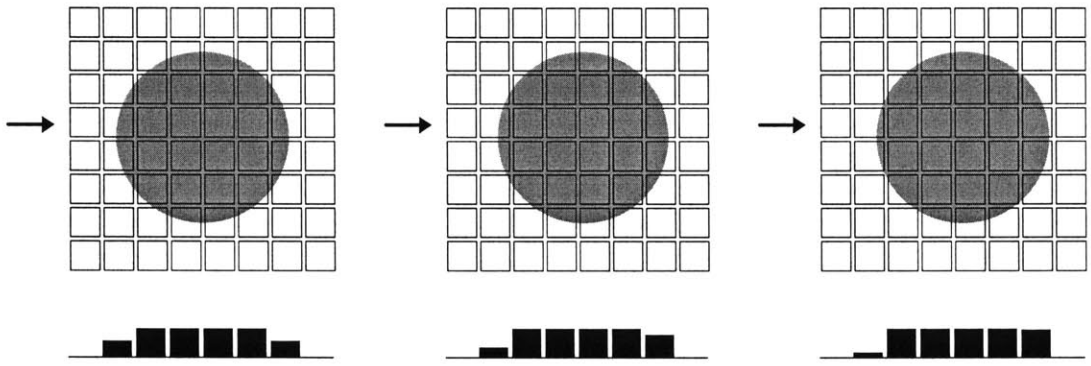

Figure 3-1: Variations in brightness caused by subpixel motions. The array of squares in each panel represents the pixels of a video camera; the gray disk represents the image of a simple scene; and the bar plots represent the brightness of the row of pixels indicated by the arrow. The three panels illustrate rightward motion of the disk. Although the displacements are subpixel (less than a pixel), information about the motion is available from changes in the brightness of the pixels near the edges. (Adapted from Freeman and Davis, 1996)

in brightness between images to estimate motion. Limits on motion resolution are different that limits on image resolution. Image resolution is usually limited to a distance on the order of the wavelength of light (550 nm for our experiment setup). Motion resolution is limited by the sensitivity and dynamic range of the video imager (a CCD in a our setup) and by the shot noise nature of light. Motions as small as two nanometers can be reliably measured. With pixels on a CCD camera on typically being 9×9 μm, the minimum resolvable motion is subpixel. Using methods originally designed for machine vision (Horn, 1986), subpixel motions are measured from changes in brightness (Figure 3-1). This technique for measuring translation is robust and precise; however, it is statistically biased. A linear bias compensation method is used to correct the bias (Davis and Freeman, 1998a).

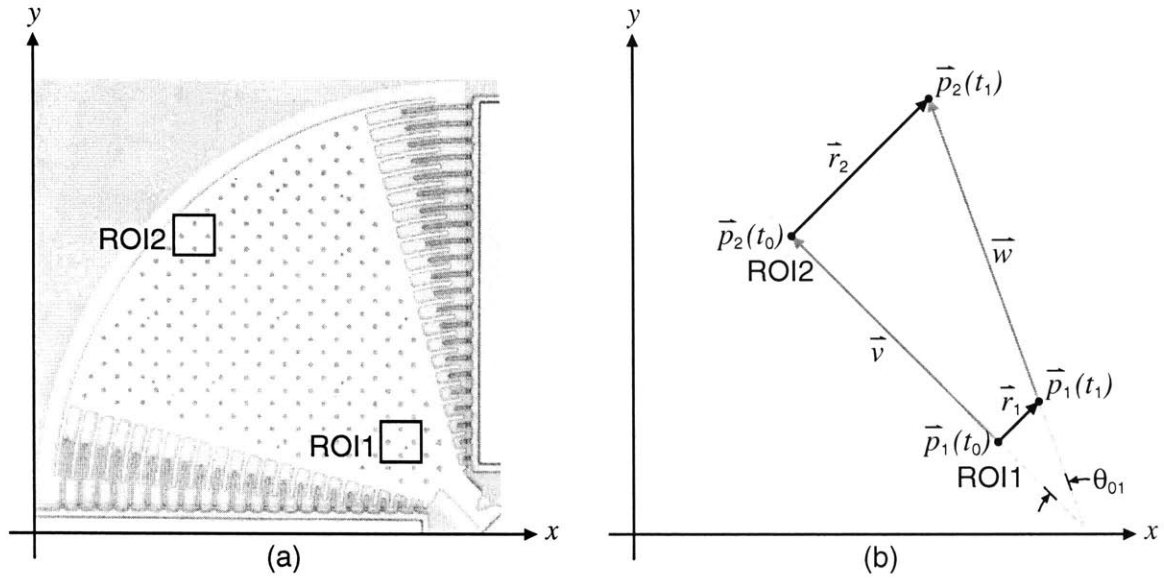

Figure 3-2: Calculating in-plane rotation from translational motion in two regions of interest (ROIs). A video image of the fatigue test structure is shown in the left panel (a) with squares indicating two ROIs. The axes show the image coordinate system. The right panel (b) shows vectors for estimating in-plane rotation θ_{01} from translational movement in the two ROIs (image omitted for clarity). The motions within each ROI are approximated as the motions of points: $\vec{p}_1(t)$ for ROI1 and $\vec{p}_2(t)$ for ROI2. The two black vectors, $\vec{r_1}$ and $\vec{r_2}$, in (b) indicate the estimated displacement of points $\vec{p}_1(t)$ and $\vec{p}_2(t)$ from their initial positions at time t_0 to their positions at time t_1. Displacements are exaggerated for clarity. Vector $\vec{v}$ connects points $\vec{p}_1(t_0)$ and $\vec{p}_2(t_0)$ and vector $\vec{w}$ connects points $\vec{p}_1(t_1)$ and $\vec{p}_2(t_1)$. The desired rotation angle θ_{01} is the angle between $\vec{v}$ and $\vec{w}$.

3.2 Rotation analysis: Using two ROIs

Translation measurements at multiple points on a rigid body can be used to estimate a rigid body's rotation. For example, 2D translation motion estimates of two regions on a rigid body can be used to estimate its rotation (Figure 3-2). We define the centers of two regions of interest (ROIs) by points $\vec{p}_1(t_0)$ and $\vec{p}_2(t_0)$. The measured translations are motions of the sections of the image within the ROIs. We approximate these motions as the motions of points $\vec{p}_1(t)$ and $\vec{p}_2(t)$. In component form, vectors $\vec{p}_1(t)$

and $\vec{p}_2(t)$ are

$$\vec{p}_1(t) = x_1(t)\ \hat{\imath} + y_1(t)\ \hat{\jmath} \tag{3.1}$$

$$\vec{p}_2(t) = x_2(t)\ \hat{\imath} + y_2(t)\ \hat{\jmath} \tag{3.2}$$

where $\hat{\imath}$ is the unit vector in the x direction and $\hat{\jmath}$ is the unit vector in the y direction. Note that the motions of points $\vec{p}_1(t)$ and $\vec{p}_2(t)$ refer to the motion of the image in ROIs 1 and 2, respectively, not the motions of the ROIs (the ROIs do not move). Both $\vec{p}_1(t)$ and $\vec{p}_2(t)$ originate at the center of their respective ROIs at time t_0.

The displacement measured between time t_0 and time t_1 in ROI1 is represented as $\vec{r}_1 = \vec{p}_1(t_1) - \vec{p}_1(t_0)$. Similarly, the motion measured in ROI2 between time t_0 and time t_1 is $\vec{r}_2 = \vec{p}_2(t_1) - \vec{p}_2(t_0)$. Vector $\vec{v}$ connects $\vec{p}_1(t_0)$ and $\vec{p}_2(t_0)$, and vector $\vec{w}$ connects $\vec{p}_1(t_1)$ and $\vec{p}_2(t_1)$:

$$\vec{v} = \vec{p}_2(t_0) - \vec{p}_1(t_0) \tag{3.3}$$

$$\vec{w} = \vec{p}_2(t_1) - \vec{p}_1(t_1)\ . \tag{3.4}$$

An estimate of the angle between the rigid body in its initial position (time t_0) and its rotated position (time t_1) is contained in the cross product of vectors v and w

$$|\vec{v} \times \vec{w}| = |\vec{v}||\vec{w}| \sin\theta_{01} \tag{3.5}$$

$$\theta_{01} = \sin^{-1}\left(\frac{|\vec{v} \times \vec{w}|}{|\vec{v}||\vec{w}|}\right)\ . \tag{3.6}$$

We use the cross product instead of the dot product to estimate θ_{01} because we want to preserve the polarity of θ_{01}. For example, in Figure 3-2(b) θ_{01} is negative if we consider counterclockwise rotations to be positive. Furthermore, the cross product is more sensitive than the dot product for small angles.

The cross product process for estimating rotation is repeated for other phases of motion. For example, if position is measured at 8 phases of motion, we can estimate rotation between each successive pair of position measurements. The sequence of incremental rotations are then used to reconstruct the device's angular position through one full cycle of motion (Figure 3-3).

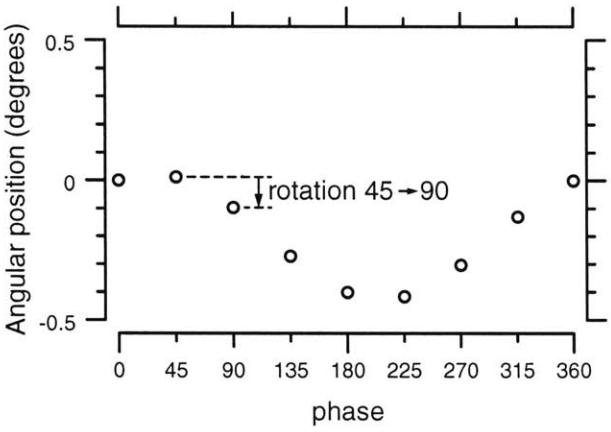

Figure 3-3: Fatigue test structure's rotation versus phase. Rotation between each phase was estimated and then summed to estimate the angular position of the device. The DC offset is due to arbitrarily assigning the first image an angular position of zero degrees.

3.3 Using many pairs of ROIs

If we place many ROIs over the rotating part of the image, many estimates of rotation can be made from all combinations of ROIs (Figure 3-4). For example, if there are 40 ROIs numbered sequentially from 1 to 40, an estimate can be made using the translation estimates in ROIs 1 and 2, ROIs 15 and 22, etc. Rotation estimates made from all possible combinations of two ROIs can be combined to give a rotation estimate with higher precision than an estimate using only one pair of ROIs.

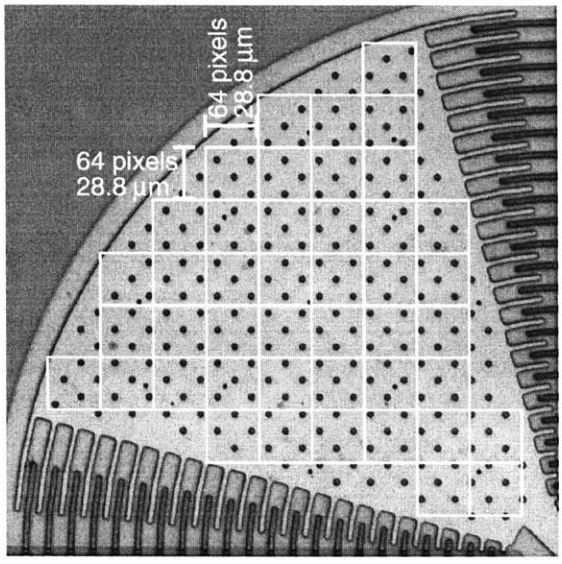

Figure 3-4: Multiple ROIs for rotational analysis. The white boxes represent the ROIs used in the rotation analysis. Their dimensions are 64×64 pixels (28.8 μm × 28.8 μm).

Issues in selecting the ROIs include how many ROIs, where to place them, and what size to make them. ROIs were defined over as much of the shuttle as possible

to maximally use the available information. Their size was chosen so that the motion in each was approximately translational and could be approximated as being located at the center of the ROI, yet they were large enough (64 pixels or 28.8 μm on a side) so that they were much bigger than the size of the motions (< 2.5 μm at maximum). The issue of ROI size is more thoroughly analyzed in the next chapter.

Rotation estimates for all pairs of ROIs are averaged. Mean and standard error for each phase of motion are computed as follows

$$\mu = \frac{1}{N}\sum_{i=1}^{N}\theta_i \tag{3.7}$$

$$\text{standard error of the mean} = \sqrt{\frac{\sum_{i=1}^{N}(\theta_i - \mu)^2}{N(N-1)}} \tag{3.8}$$

$$= \sqrt{\frac{N\sum{\theta_i}^2 - \left(\sum\theta_i\right)^2}{N^2(N-1)}} \tag{3.9}$$

where θ_i are the individual rotation estimates from each ROI pair and N is the total number of ROI pairs.

3.3.1 Results using many pairs of ROIs

The fatigue test structure was driven at resonance and images were taken at evenly spaced intervals through its sinusoidal motion. Rotation between each pair of consecutive images was calculated by Equations 3.6 and 3.7. Rotation for each phase of motion were then summed to reconstruct the fatigue test structure's angular position through one full cycle of motion as in Figure 3-3. We use an FFT to compute the peak-to-peak average rotation. Appendix A shows a derivation of how the error in each phase of rotation (from Equation 3.8) propagates through the formula for an FFT to give error in the peak-to-peak value. The peak-to-peak rotation of the fatigue test structure at resonance is 0.4291 ± 0.00160 degrees p-p.

3.4 Statistics of Pairwise Rotation Analysis

In the previous section we averaged rotation estimates from many ROI pairs. This procedure would be optimal if the errors in each estimate were statistically independent and identically distributed. However, error varies greatly between estimates. First we analyze physical mechanisms that give rise to errors in rotation estimates. We then construct a weighted average with weights chosen to reduce the relative contributions of ROI pairs that are likely to be in error.

3.4.1 Fixed pattern noise

In computer microvision measurements, a major source of error is from fixed pattern noise: structure in the image that does not move with the image. Dirt on the optics and nonuniform sensitivities of pixels in the camera contribute to fixed pattern noise.

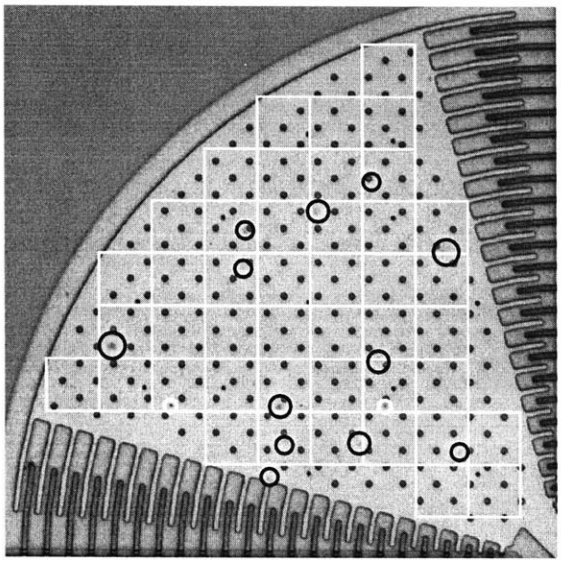

Figure 3-5: Fixed pattern noise. The picture shows the ROIs used to estimate rotation as white squares. The black circles enclose regions with high fixed pattern noise, probably due to dirt on the optics. These regions were hand selected by viewing a sequence of images taken at different phases of motion and picking out features that remained stationary while the shuttle moved. The smaller white circles in enclose spots that move with the shuttle. Presumably, they are specks of dirt on the surface of the shuttle, which would not interfere with motion estimation.

The black circles in Figure 3-5 enclose regions with high fixed pattern noise, probably due to dirt on the optics. These noisy regions were hand selected by viewing a sequence of images taken at different phases of motion and picking out features that remained stationary while the shuttle moved. The smaller white circles in Figure 3-5 enclose specks of dirt on the shuttle. Dirt which lies on the shuttle's surface does not

interfere with the motion analysis.

Dirt on the optics should be more easily visible in an image of a mirror. To determine the level of fixed pattern noise throughout the data images, we take a background picture of a mirror (top panel Figure 3-6). Ideally, the background picture should be a constant brightness. However, the same fixed pattern noise that shows up in the data images appears in the background picture. Some specks in the background picture may be due to dirt on the mirror which can be confused with fixed pattern noise. Efforts were taken to keep the mirror clean.

The standard deviation of pixel brightness within each ROI was calculated as a measure of fixed pattern noise. The bottom of Figure 3-6 shows a histogram of the standard deviation of brightness for all ROIs. Since dirt appears nearly black and the rest of the image is a flat gray, ROIs which contained dirt tended to have high standard deviations. Knowledge of the fixed pattern noise in each ROI will be used as part of the weighted average.

3.4.2 Inter-ROI distance

In this section we show that the error in rotation estimates from ROIs in close proximity to each other is larger than that from ROIs further apart. The basis for this argument comes from the way errors in the translation estimates contribute to error in the rotation estimate.

Shown in Figure 3-7 are translation estimates, r_1 and r_2, of two points, $\vec{p}_1(t_0)$ and $\vec{p}_2(t_0)$. The rotation angle θ is the angle between the line connecting the points at time t_0 and the line connecting the points at time t_1, and d is the distance between points $\vec{p_1}$ and $\vec{p_2}$ in their initial positions. If the translation estimates r_1 and r_2 are affected by noise processes so that the variances of the estimates are ${\sigma_{r_1}}^2$ and ${\sigma_{r_2}}^2$, respectively, we can compute the variance of the rotation estimate, θ as follows. There is a trigonometric relation between θ, r_1, and r_2

$$\tan\theta = \frac{r_2 - r_1}{d} \ . \tag{3.10}$$

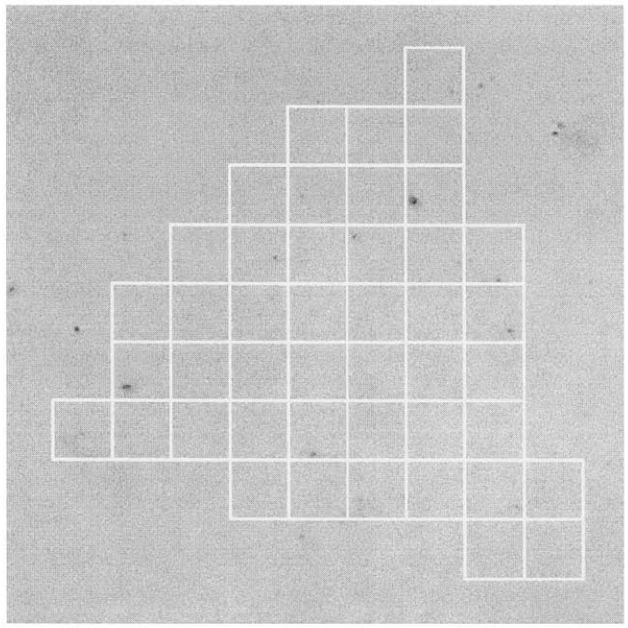

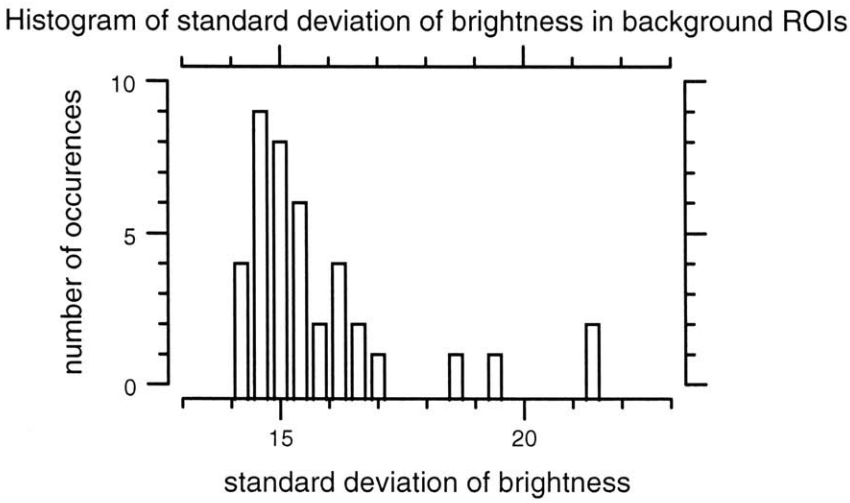

Figure 3-6: Fixed pattern noise in a background image. The background image (top) is an image of a mirror. The white squares show the ROIs from Figure 3-4. Nonuniformity in brightness across pixels represents fixed pattern noise that results, for example, from dirt on optics or nonuniform sensitivities of pixels in the camera. The standard deviation of brightness within each ROI was calculated as a measure of fixed pattern noise.

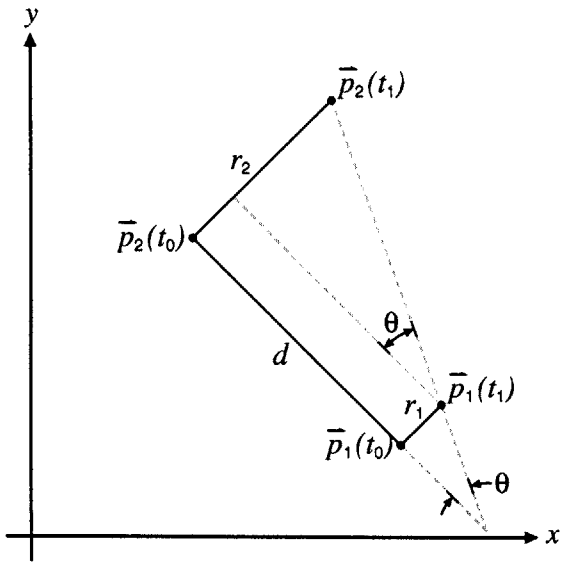

Figure 3-7: Error in rotation estimate due to error in translation estimate. Distances r_1 and r_2 are translation estimates of points $\vec{p}_1(t_0)$ and $\vec{p}_2(t_0)$. The distance between points $\vec{p}_1(t_0)$ and $\vec{p}_2(t_0)$ is d, also called the inter-ROI distance. Rotation angle $\theta = \tan^{-1}\left(\frac{r_2 - r_1}{d}\right) \approx \frac{r_2 - r_1}{d}$.

We can make the small angle approximation $\tan\theta = \theta$ since the angles being measured are small,

$$\theta \approx \frac{r_2 - r_1}{d} \ . \tag{3.11}$$

If errors in the estimate of r_1 are independent of those for r_2 the variance of the rotation estimate θ is

$$\sigma_\theta^2 = \frac{1}{d^2}(\sigma_{r_2}^2 + \sigma_{r_1}^2) \ . \tag{3.12}$$

The variance of the translation estimates ${\sigma_{r_1}}^2$ and ${\sigma_{r_2}}^2$ are proportional to the fixed pattern noise in each ROI,

$$\sigma_{r_1}^2 = k\sigma_{f_1}^2 \tag{3.13}$$

$$\sigma_{r_2}^2 = k\sigma_{f_2}^2 \tag{3.14}$$

where ${\sigma_{f_1}}^2$ and ${\sigma_{f_2}}^2$ represent the fixed pattern noise in ROIs 1 and 2, respectively, and k is a proportionality constant. Equations 3.13 and 3.14 hold only for fixed pattern noise energy levels between -40 and -20 dB relative to mean energy in the image which is our operating range (Figure 7 in Davis and Freeman, 1998a). Now,

Equation 3.12 becomes

$$\sigma_\theta{}^2 = \frac{k}{d^2}(\sigma_{f_2}^2 + \sigma_{f_1}^2) \tag{3.15}$$

$$= \frac{k\sigma_f^2}{d^2} \tag{3.16}$$

where $\sigma_f{}^2$ is the sum of the fixed pattern noise in ROIs 1 and 2. Equation 3.16 predicts that the variance of rotation estimates is proportional to the variance of fixed pattern noise and inversely proportional to the square of distance between ROIs.

We now verify that Equation 3.16 holds for data. Rotation estimates from all pairs of ROIs are plotted versus their inter-ROI distance in Figure 3-8. The estimates from ROI pairs with small inter-ROI distance have higher variance than estimates from ROI pairs with larger inter-ROI distances.

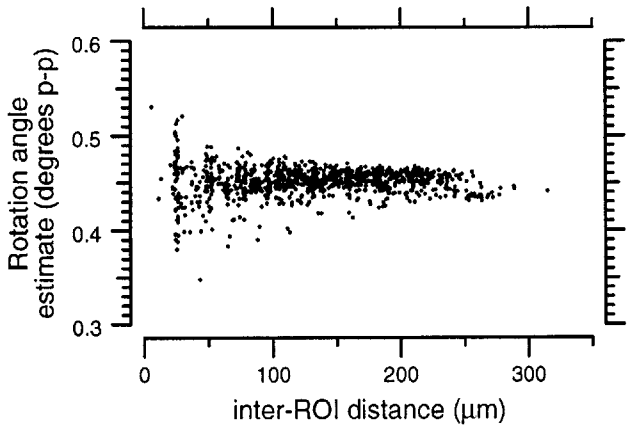

Figure 3-8: Rotation estimates as a function of inter-ROI distance. Each dot represents a rotation estimate from a pair of ROIs plotted versus the distance between the pair of ROIs.

To experimentally test that the standard deviation of rotation estimates is inversely proportional to inter-ROI distance d as theorized in Equation 3.16, we need an estimate of the variance of each rotation estimate. However, the variance for each data point is not available. Instead, the points in Figure 3-8 were placed into bins with approximately 30 points each. The standard deviations of the points in each bin were plotted versus distance (Figure 3-9). A $1/d$ curve is also shown. Any variation in the data away from the $1/d$ curve is may be due to the variation of $\sigma_f{}^2$ between data points.

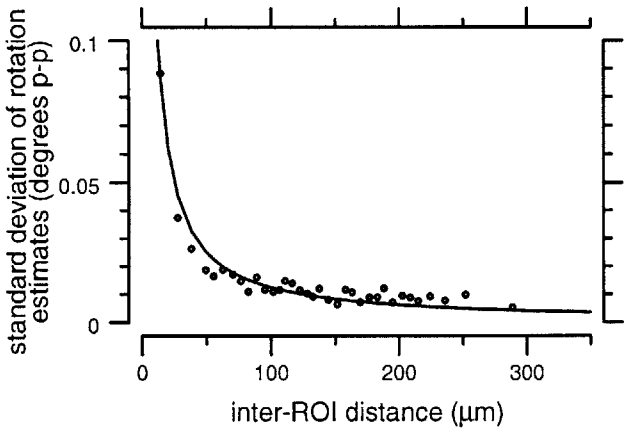

Figure 3-9: Variation of standard deviation of rotation estimates with inter-ROI distance. The rotation estimates in Figure 3-8 were separated into bins with 30 points each across inter-ROI distance. A $1/d$ curve is also shown.

Weighted mean

If we have N independent rotation estimates, $\theta_1, \theta_2, \ldots, \theta_{N-1}, \theta_N$, each with variance ${\sigma_1}^2, {\sigma_2}^2, \ldots, {\sigma_{N-1}}^2, {\sigma_N}^2$, the minimum variance weighted average is (Bevington and Robinson, 1992):

$$\mu_w = \frac{\sum_{i=1}^{N} (\theta_i / \sigma_{\theta_i}^2)}{\sum_{i=1}^{N} (1/\sigma_{\theta_i}^2)} \,. \tag{3.17}$$

By Equation 3.16

$$\mu_w = \frac{\sum \frac{{d_i}^2 \theta_i}{k\sigma_f^2}}{\sum \frac{{d_i}^2}{k\sigma_f^2}} = \frac{\sum \frac{{d_i}^2 \theta_i}{\sigma_f^2}}{\sum \frac{{d_i}^2}{\sigma_f^2}} = \frac{\sum w_i \theta_i}{\sum w_i} \tag{3.18}$$

where each angle estimate θ_i is weighted by the a weighting factor

$$w_i = \frac{{d_i}^2}{\sigma_f^2} \,. \tag{3.19}$$

Rotation estimates with small inter-ROI distances or large fixed pattern noise receive less weight in Equation 3.18. Conversely, rotation estimates with large inter-ROI distances or small fixed pattern noise receive more weight in Equation 3.18.

The standard error of the weighted mean or the variance in the weighted mean is

(Bevington and Robinson, 1992):

$$\sigma^2_{\mu_w} = \left(\frac{\sum w_i {\theta_i}^2}{\sum w_i} - {\mu_w}^2 \right) \times \frac{1}{N-1} \tag{3.20}$$

$$= \left(\frac{\sum w_i {\theta_i}^2}{\sum w_i} - \left(\frac{\sum w_i \theta_i}{\sum w_i} \right)^2 \right) \times \frac{1}{N-1} \tag{3.21}$$

$$\begin{matrix} \text{standard error} \\ \text{of the weighted mean} \end{matrix} = \sqrt{\left(\frac{\sum w_i {\theta_i}^2}{\sum w_i} - \left(\frac{\sum w_i \theta_i}{\sum w_i} \right)^2 \right) \times \frac{1}{N-1}} \,. \tag{3.22}$$

If all the inter-ROI distances were equal, Equation 3.22 simplifies to the formula for the standard error of an unweighted mean (Equation 3.9). Equation 3.18 computes a weighted average which takes the statistical properties of errors into account and Equation 3.22 computes the error in the weighted average so we can see if its precision is better than that of the unweighted average.

3.4.3 Weighted mean results

Two data sets are used. The first consists of 8 images acquired during sinusoidal stimulation of the fatigue test structure. Peak-to-peak rotation is reported. The second consists of 10 images of the fatigue test structure mounted on a calibrated rotation stage. Pairwise analysis of these images produces rotation estimates that can be compared to stage rotation determined from a micrometer.

Peak-to-peak results

The unweighted average rotation and weighted average peak-to-peak rotation are reported for the same data set in Table 3.1. The rotation estimate changed negligibly while the precision improved by nearly 50%. Using the weighted average, peak-to-peak rotation can be measured to a precision of roughly 1 millidegree p-p.

Table 3.1: Peak-to-peak weighted mean rotation estimates

Statistics (degrees p-p)	Unweighted Mean	Weighted Mean	Change
Mean rotation estimate	0.4291	0.4296	0.12%
Standard error of the mean	0.00160	0.00091	-43%

Calibration results

To determine the accuracy of the method, we attached the fatigue test structure to a rotation stage (Newport Model 37, Irvine, CA) accurate to 0.7 millidegrees. We rotated the device to known positions and took pictures of the device. Rotation estimates were also derived from the images using ROI pairs with weighted averaging. Rotation estimates are plotted versus rotation stage position in the top panel of Figure 3-10. It is important to note that these results are not peak-to-peak rotations; each point represents the rotation measured between two images.

The bottom plot in Figure 3-10 shows the difference between the estimated angle and the reference angle; it the accuracy of the rotation estimates. The error in Figure 3-10 is calculated according to

$$\text{error (accuracy)} = \theta_e - \theta_r \tag{3.23}$$

where θ_e is the estimated angle and θ_r is the reference angle. Both θ_e and θ_r are not exact. θ_e has a limited precision given by Equation 3.22 and θ_r is inexact due to error in the stage micrometer. The precision in the estimated angle is 0.2 millidegrees for the smallest measured angle and 0.7 millidegrees for the largest measured angle. The error in the rotation stage is 0.7 millidegrees. The error bars on the error in the bottom panel of Figure 3-10 arise due to the the precision of θ_e and the error in θ_r. Essentially, it's the error in the error of Equation 3.23:

$$\text{error bar size (precision)} = \sigma^2_{\theta_e} + \sigma^2_{\theta_r} \tag{3.24}$$

Equation 3.23 defines what we mean by accuracy and Equation 3.24 defines preci-

sion. Over the range of tested angles (±1 degree), the estimates are accurate to ±5 millidegrees and precise to ±1 millidegree. Accuracy and precision are summarized in Table 3.2.

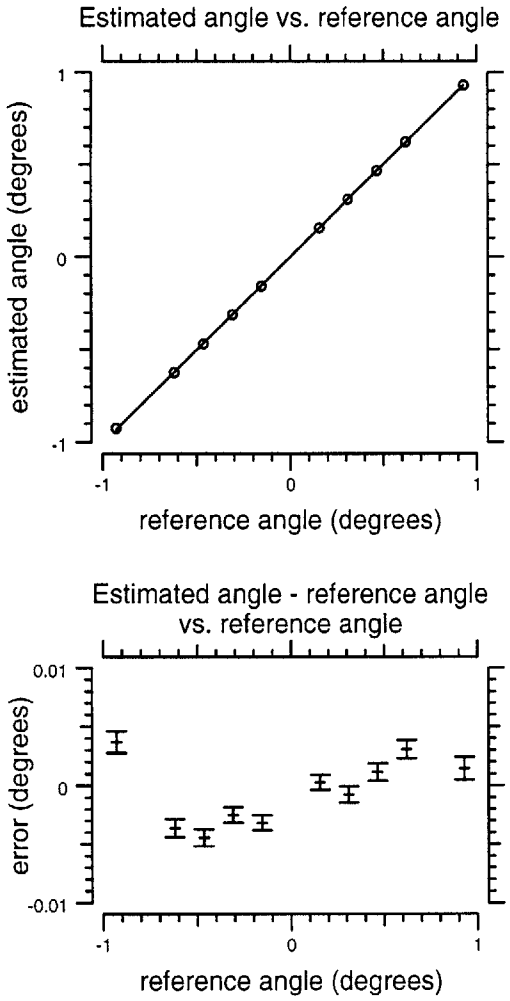

Figure 3-10: Calibration results. Angles were estimated from 10 images using the weighted mean. The top plot shows the linearity of the estimated angle versus the stage's reference position. The slope of the regression line is 1.0018. The bottom plot shows the difference between the estimated angle and the reference angle. The error bars around the points are the sum of the error in reference angle (0.7 millidegrees) and the precision in the estimated angle (between 0.2 and 0.7 millidegrees). Accuracy of the estimates is roughly 5 millidegrees and precision is roughly 1 millidegree.

Table 3.2: Accuracy and precision of rotation estimates over ±1 degree

Accuracy	Precision
5 millidegrees (18 arcsec)	1 millidegree (3.6 arcsec)

Measuring rotation by weighted average of rotation estimates from many pairs of ROIs is accurate to 5 millidegrees and precise to 1 millidegree. However, these results took more that 10 minutes on a Pentium 450 MHz computer with 128 MB of RAM.

Computation time roughly goes as the number (N) of ROIs squared since the number of distinct pairs is $\frac{N(N-1)}{2}$. As shown in Figure 3-4, we used 44 ROIs which means there are 946 distinct ROI pairs. The number of ROIs we use in pairwise analysis can seriously affect computation time.

While pairwise rotation analysis is accurate and reliable in the presence of fixed pattern noise, we desire faster method. The next chapter explores a faster method for measuring rotation which also uses the translation estimates from many ROIs. We also discuss the effects of using different size ROIs.

Chapter 4

Measuring Rotation: Least Squares Estimator

The previous chapter developed a method for estimating rigid body rotations by pairwise analysis of translations of multiple regions of interest distributed over the body. The resulting technique is robust, but it is ad hoc, computationally intensive, and statistically difficult to evaluate with regard to error and bias. This chapter describes a new method in which information from multiple ROIs is combined in a least squares sense.

First we describe the the fundamentals of the method and derive relevant formulas. Next, we discuss how to use the method and how to set necessary parameters, such as ROI size and ROI placement. We also give experimental results in this section.

4.1 Rotation using the least squares method

As with the previous method, our goal is to estimate rigid body rotation from estimates of the translations of many points on the rigid body. Rigid body rotations can be determined from the translation of any two points on the rigid body. In the previous method, rotations from all pairs of points were averaged. In the new method, a single rotation is obtained from the translations of many points. Since only two points are needed to estimate rotation, estimates based on more than two are over-

constrained. Furthermore, noise in the translation esitimates leads to inconsistency of rotations based on different sets of points. In the new method, the overconstrained problem of estimating rotation from translations of three or more points is solved using a least squares approach. The idea is to find the rotation estimate that is most consistent with all of the point translations.

Like many least squares estimators, we describe an error term associated with each translation estimate which contains the rotation angle we want to estimate. Then we square the error term for each translation estimate and add them. Minimizing this accumulated error term with respect to the rotation angle is the last step. After we have calculated the rotation angle which minimizes the accumulated error, we can compute the accumulated error in order to see how it changes as we vary parameters such as ROI size, ROI placement, etc.

Since the fatigue test structure is assumed rigid, the translation estimate in each ROI can be equated to an overall translation and rotation of the fatigue test structure. We can choose the center of rotation arbitrarily because the rotation is constant regardless of reference frame. With respect to the center of rotation, we define the position of the section of the first image in the ith ROI as $\vec{r_{i1}} = \begin{bmatrix} x_{i1} \\ y_{i1} \end{bmatrix}$. We then estimate the translation $\vec{dr_i} = \begin{bmatrix} dx_i \\ dy_i \end{bmatrix}$ in this image region between the first and second images. Then the new position is $\vec{r_{i2}} = \begin{bmatrix} x_{i2} \\ y_{i2} \end{bmatrix} = \begin{bmatrix} x_{i1} \\ y_{i1} \end{bmatrix} + \begin{bmatrix} dx_i \\ dy_i \end{bmatrix}$ in the second image.

The estimated overall translation of the entire fatigue test structure is defined as $\vec{r_s} = \begin{bmatrix} x_s \\ y_s \end{bmatrix}$ and the estimated rotation angle is θ. Position vectors $\vec{r_1}$ and $\vec{r_2}$ are related by (Foley et al., 1990) (Figure 4-1)

$$\vec{r_{i2}} = \begin{bmatrix} \cos\theta & -\sin\theta \\ \sin\theta & \cos\theta \end{bmatrix} \vec{r_{i1}} + \vec{r_s} \tag{4.1}$$

$$\begin{bmatrix} x_{i2} \\ y_{i2} \end{bmatrix} = \begin{bmatrix} \cos\theta & -\sin\theta \\ \sin\theta & \cos\theta \end{bmatrix} \begin{bmatrix} x_{i1} \\ y_{i1} \end{bmatrix} + \begin{bmatrix} x_s \\ y_s \end{bmatrix} . \tag{4.2}$$

We make the small angle approximation $\sin\theta \approx \theta$ which gives

$$\begin{bmatrix} x_{i2} \\ y_{i2} \end{bmatrix} = \begin{bmatrix} 1 & -\theta \\ \theta & 1 \end{bmatrix} \begin{bmatrix} x_{i1} \\ y_{i1} \end{bmatrix} + \begin{bmatrix} x_s \\ y_s \end{bmatrix} \tag{4.3}$$

$$\begin{bmatrix} x_{i2} \\ y_{i2} \end{bmatrix} = \begin{bmatrix} x_{i1} - \theta y_{i1} + x_s \\ \theta x_{i1} + y_{i1} + y_s \end{bmatrix} . \tag{4.4}$$

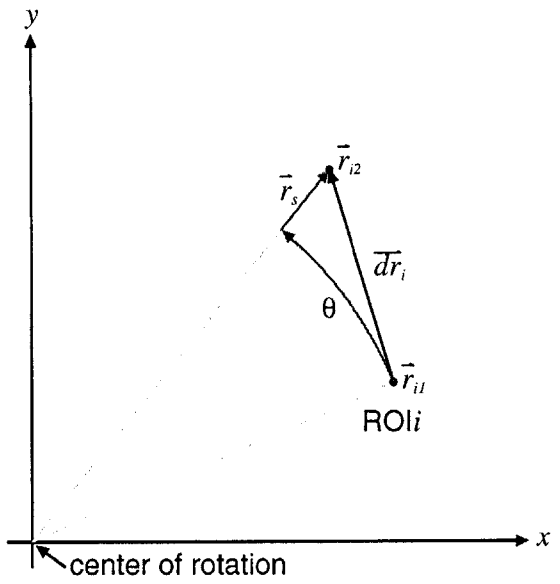

Figure 4-1: Least squares rotation estimate. The black vector $\vec{dr}_i$ indicates the estimated translation for ROI i. The estimated translation in ROI i can be equated to rotation θ around the origin and a translation indicated by vector $\vec{r}_s$.

The same value of rotation (θ) and translation ($\begin{bmatrix} x_s \\ y_s \end{bmatrix}$) will not satisfy Equation 4.4 for all ROIs since there is noise in the measurements. We define the error between the estimated position of ROI i in the second image $\begin{bmatrix} x_{i2} \\ y_{i2} \end{bmatrix}$ and the new position of ROI i in the first image due to the overall translation $\begin{bmatrix} x_s \\ y_s \end{bmatrix}$ and rotation θ of the fatigue test structure as

$$e_i = \begin{bmatrix} x_{i2} \\ y_{i2} \end{bmatrix} - \begin{bmatrix} x_{i1} - \theta y_{i1} + x_s \\ \theta x_{i1} + y_{i1} + y_s \end{bmatrix} \tag{4.5}$$

$$e_i = \begin{bmatrix} x_{i2} - x_{i1} + \theta y_{i1} - x_s \\ y_{i2} - \theta x_{i1} - y_{i1} - y_s \end{bmatrix} . \tag{4.6}$$

We note that $x_{i2} - x_{i1} = dx_i$ and $y_{i2} - y_{i1} = dy_i$ and have

$$e_i = \begin{bmatrix} dx_i + y_{i1}\theta - x_s \\ dy_i - x_{i1}\theta - y_s \end{bmatrix} . \tag{4.7}$$

The accumulated error for all the ROIs is the sum of squares of all e_i's, ($^{\mathrm{T}}$ means transpose)

$$E = \sum_{i=1}^{N} e_i{}^{\mathrm{T}} e_i = \sum_{i=1}^{N} \left((dx_i + y_{i1}\theta - x_s)^2 + (dy_i - x_{i1}\theta - y_s)^2 \right) . \tag{4.8}$$

The accumulated error E is referred to as the "squared error". To minimize E with respect to the rotation angle θ, we need to differentiate E with respect to θ. However, θ is not the only unknown in Equation 4.8. The overall translation of the fatigue test structure, x_s and y_s, is also not known. We'll need to differentiate E with respect to x_s and y_s in order to fully solve for θ. The following equations are E differentiated with respect to x_s, y_s, and θ.

$$\frac{\partial E}{\partial x_s} = \sum (-2(dx_i - x_s + y_{i1}\theta)) \tag{4.9}$$

$$\frac{\partial E}{\partial y_s} = \sum (-2(dy_i - y_s - x_{i1}\theta)) \tag{4.10}$$

$$\frac{\partial E}{\partial \theta} = \sum (2(dx_i - x_s + y_{i1}\theta)y_i - 2(dy_i - y_s - x_{i1}\theta)x_i) \tag{4.11}$$

We set Equations 4.9 through 4.11 equal to zero and solve for θ, x_s, and y_s:

$$\theta = \frac{N\sum dx_i y_i - \sum dx_i \sum y_i - N\sum dy_i x_i + \sum dy_i \sum x_i}{(\sum y_i)^2 - N\sum {y_i}^2 + (\sum x_i)^2 - N\sum {x_i}^2} \tag{4.12}$$

$$x_s = \frac{1}{N}(\sum dx_i + \theta \sum y_i) \tag{4.13}$$

$$y_s = \frac{1}{N}(\sum dy_i - \theta \sum x_i) . \tag{4.14}$$

After we calculate x_s, y_s, and θ, we can compute the squared error E as a goodness measure of the rotation angle estimate,

$$\begin{aligned} E = & \sum {dx_i}^2 + \sum {dy_i}^2 + N({x_s}^2 + {y_s}^2) + \\ & \theta^2(\sum {x_i}^2 + \sum {y_i}^2) - 2x_s \sum dx_i - 2y_s \sum dy_i + \\ & 2\theta(\sum dx_i y_i - x_s \sum y_i - \sum dy_i x_i + y_s \sum x_i) \ . \end{aligned} \tag{4.15}$$

A more meaningful error metric is the root mean square (rms) error:

$$E_{\text{rms}} = \sqrt{E/N} \ . \tag{4.16}$$

The rms error tells us, on average, how well (in pixels) the translation estimate for each ROI matches the rigid body rotation estimated by x_s, y_s, and θ. A good least squares fit should have an rms error less than approximately 0.1 pixels.

4.1.1 Weighted least squares

If we know what the fixed pattern noise is in each ROI, we can improve the rotation estimate by weighting each error term in Equation 4.8 by the inverse of the fixed pattern noise ($\sigma_{f_i}^2$) in that ROI:

$$E_w = \sum_{i=1}^{N} \frac{1}{\sigma_{f_i}^2} {e_i}^{\mathrm{T}} e_i \tag{4.17}$$

$$E_w = \sum_{\text{all } i} \frac{1}{\sigma_{f_i}^2} \left((dx_i - x_s + y_{i1}\theta)^2 + (dy_i - y_s - x_{i1}\theta)^2 \right) \ . \tag{4.18}$$

If we follow the same derivation as in Equations 4.9 through 4.11 we find

$$\theta = \frac{\sum \frac{1}{\sigma_{f_i}^2} \sum \frac{dx_i y_i}{\sigma_{f_i}^2} - \sum \frac{dx_i}{\sigma_{f_i}^2} \sum \frac{y_i}{\sigma_{f_i}^2} - \sum \frac{1}{\sigma_{f_i}^2} \sum \frac{dy_i x_i}{\sigma_{f_i}^2} + \sum \frac{dy_i}{\sigma_{f_i}^2} \sum \frac{x_i}{\sigma_{f_i}^2}}{(\sum \frac{y_i}{\sigma_{f_i}^2})^2 - \sum \frac{1}{\sigma_{f_i}^2} \sum \frac{{y_i}^2}{\sigma_{f_i}^2} + (\sum \frac{x_i}{\sigma_{f_i}^2})^2 - \sum \frac{1}{\sigma_{f_i}^2} \sum \frac{{x_i}^2}{\sigma_{f_i}^2}} \tag{4.19}$$

$$x_s = \frac{\sum \frac{dx_i}{\sigma_{f_i}^2} + \theta \sum \frac{y_i}{\sigma_{f_i}^2}}{\sum \frac{1}{\sigma_{f_i}^2}} \tag{4.20}$$

$$y_s = \frac{\sum \frac{dy_i}{\sigma_{f_i}^2} - \theta \sum \frac{x_i}{\sigma_{f_i}^2}}{\sum \frac{1}{\sigma_{f_i}^2}} \; . \tag{4.21}$$

We can also calculate the error for the weighted least squares result:

$$\begin{aligned} E_w = & \sum \frac{{dx_i}^2}{\sigma_{f_i}^2} + \sum \frac{{dy_i}^2}{\sigma_{f_i}^2} + \sum \frac{1}{\sigma_{f_i}^2}({x_s}^2 + {y_s}^2) + \\ & \theta^2(\sum \frac{{x_i}^2}{\sigma_{f_i}^2} + \sum \frac{{y_i}^2}{\sigma_{f_i}^2}) - 2x_s \sum \frac{dx_i}{\sigma_{f_i}^2} - 2y_s \sum \frac{dy_i}{\sigma_{f_i}^2} + \\ & 2\theta(\sum \frac{dx_i y_i}{\sigma_{f_i}^2} - x_s \sum \frac{y_i}{\sigma_{f_i}^2} - \sum \frac{dy_i x_i}{\sigma_{f_i}^2} + y_s \sum \frac{x_i}{\sigma_{f_i}^2}) \; . \end{aligned} \tag{4.22}$$

Again, a more meaningful error metric is the root mean square (rms) error:

$$E_{w,\text{rms}} = \sqrt{E_w / N} \; . \tag{4.23}$$

Using translation estimates from many ROIs and Equations 4.19 and 4.23 we can compute a least squares estimate for rotation and gauge how good it is.

4.2 Results and setting parameters

In this section we look at results using different size ROIs. The ROIs should be small enough so the motion in the region it encompasses can be approximated as translational. Conversely, the ROIs should be large enough so that the magnitude of motion is significantly smaller than the dimensions of the ROI. If the ROI is too small the image might move completely out of the ROI from one time increment to the next. For example, if the image in a ROI moves 20 pixels but the ROI is only 15 pixels wide the image in the ROI at two consecutive time increments will be completely different. ROIs that are too small can lead to an unpredictably wrong translation estimates. Also, if too few pixels are included, the error in the translation estimate will be large. Using large ROIs also improves accuracy of translation estimates. At 1 degree of rotation, the biggest motion in of the shuttle is less than 10 pixels. Under

these constraints, ROIs should be bigger than 20 pixels on a side.

ROIs of various sizes were placed over as much of the surface of the fatigue test structure as possible because we want to use all information to most accurately estimate rotation. Also, in order to make reasonable comparisons between results from different size ROIs, we want to cover the same area with each size ROI. Unfortunately, as ROI size goes up, the number of ROIs needed to cover the shuttle of the fatigue test structure goes down.

We used square ROIs ranging in size from 20 pixels on a side (400 total pixels) to 200 pixels on a side (40000 total pixels). For 10 different angles ranging from -1 to $+1$ degree, the fatigue test structure was rotated on the Newport rotation stage to an accuracy of 0.7 millidegrees. The absolute differences between the estimated angles and the reference (true) angles are plotted for each ROI size in Figure 4-2. Larger errors occur with larger rotations. There is a range in ROI sizes from 3600 to 14400 total pixels (60 to 120 pixels on a side) where the absolute errors for all rotation estimates are less than 10 millidegrees.

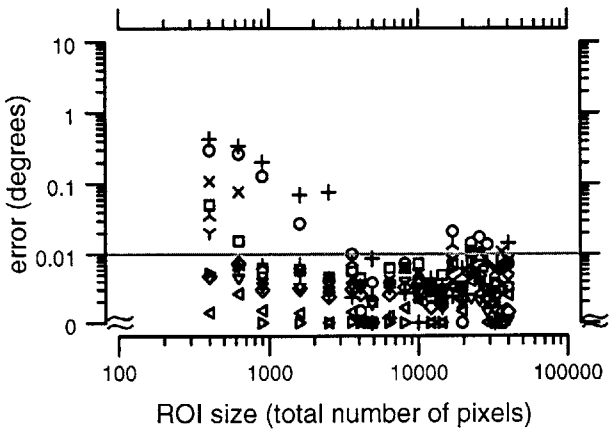

Figure 4-2: Error versus ROI size. Absolute error between estimated angle (using the LSM method) and the reference angle is plotted versus ROI size for 10 different angular displacements ranging from -1 to $+1$ degree. Larger errors occur for larger angles. Accuracy below 10 millidegrees is attainable using ROI sizes between 3600 pixels and 14400 pixels (60 pixels on a side and 120 pixels on a side).

Summary

Rotation can be measured accurately over a range of ± 1 degrees to 10 millidegrees. The computation time is over an order of magnitude less than using the "ROI pairs" estimator in the last chapter.

Chapter 5

Conclusions and Discussion

In this thesis, we developed a method for accurately and precisely measuring in-plane rotation of a MEMS device using computer microvision. In Chapter 2 we described the experimental apparatus and technique for collecting data. Video microscopy is used with strobe illumination to collect a sequence of images which are later analyzed.

Then in Chapter 3 we discussed our group's previous work on estimating translational motion from a series of images and described how we use estimated translation motion at a pair of ROIs to measure rotation of a rigid body. We averaged the rotation estimates from each pair of ROIs to produce a precise estimate of rotation. However, fixed pattern noise and translation measurement noise corrupted the rotation measurements. Knowledge of the nature of these noise sources led to a more precise weighted rotation estimator that is less sensitive to fixed pattern noise and translation measurement noise. The weighted rotation estimator is a weighted average of the rotation estimates from each pair of ROIs. The weighting factor is the square of the ratio between the inter-ROI distance and the fixed pattern noise.

In Chapter 4 another rotation measurement scheme was developed using a least squares approach. The least squares rotation estimator gives one rotation estimate from many translation estimates, whereas the ROI pairs method of Chapter 3 averages rotation estimates from many pairs of ROIs. In the least squares approach, we described an error term involving translation estimates from many ROIs which we minimized with respect to the desired rotation angle. To lessen the technique's

sensitivity to fixed pattern noise, we used the inverse of the fixed pattern noise as a weighting factor in the error term. The weighted least squares method proved to be less ad hoc, statistically easier to evaluate and computationally less expensive than the ROI pairs method described in Chapter 3.

Using either measurement technique described above, rotation was measured over a range of $\pm$ 1 degree to an accuracy of 10 millidegrees and a precision of 1 millidegree. Figure 5-1 illustrates the microscopic size of the method's accuracy.

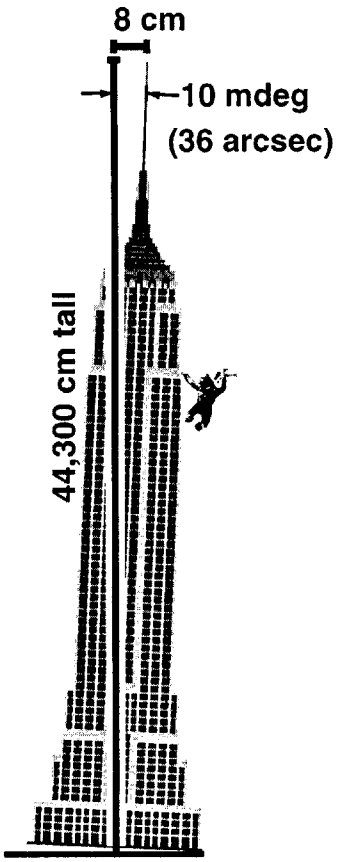

Figure 5-1: Illustrating the method's excellent accuracy. If the Empire State Building in New York City tilted an angle of 10 millidegrees from the zenith, the building's top would only move 8 centimeters from its upright position.

Robust rotation analysis of the fatigue test structure has improved computer microvision by expanding its capabilities from accurate translation measurements to robust, accurate rotation measurements. This method can be extended into three dimensions and used to measure the two out-of-plane angles (pitch and roll). This rotation measurement technique can be applied to other MEMS devices as well. Machines with parts sweeping out small angles like microgears or micromirrors for display devices or fiber optic switches are particularly well suited for this technique.

Appendix A

Error in an FFT

A fast Fourier transform (FFT) is a computationally fast way of computing a discrete Fourier transform (DFT). In analyzing how error propogates through the FFT, we will arrive at the same answer if we analyze the DFT instead. The formula for a DFT is

$$X[k] = \sum_{n=0}^{N-1} x[n] e^{-j\frac{2\pi}{N}kn} \tag{A.1}$$

$$= \sum_{n=0}^{N-1} x[n]\cos(\tfrac{2\pi}{N}kn) - j\sum_{n=0}^{N-1} x[n]\sin(\tfrac{2\pi}{N}kn) \tag{A.2}$$

$$= Re\{X[k]\} + jIm\{X[k]\} \tag{A.3}$$

where $x[n]$ are the rotation estimates for each phase of rotation and $X[k]$ are the DFT coefficients. When dealing with sinusoidal motion, we are usually only interested in one DFT coefficient—$X[1]$ if we are looking at the fundamental, $X[2]$ if we are interested in the second harmonic, etc. The inverse relationship is as follows

$$x[n] = \frac{1}{N}\sum_{k=0}^{N-1} X[k] e^{j\frac{2\pi}{N}kn} \tag{A.4}$$

$$= \frac{X[0]}{N} + \frac{2}{N}\sum_{k=1}^{\frac{N}{2}-1} |X[k]|\cos(\tfrac{2\pi}{N}kn + \angle X[k]) + \frac{1}{N}X[\tfrac{N}{2}]\cos(n\pi) \quad \text{(N even)} \tag{A.5}$$

where we are usually only interested in DFT coefficients for $1 < k < \frac{N}{2} - 1$. For this case, the peak-to-peak value is

$$A[k] = \tfrac{4}{N}|X[k]| \tag{A.6}$$

and the phase is

$$P[k] = \angle X[k] \tag{A.7}$$

for a particular harmonic k. If $x[n]$ is purely sinusoidal at harmonic k we can represent $x[n]$ as

$$x[n] = \frac{A[k]}{2}\cos(\tfrac{2\pi}{N}kn + P[k]) \ . \tag{A.8}$$

The variance in the peak-to-peak value $A[k]$ is

$$\sigma^2_{A[k]} = \tfrac{16}{N^2}\sigma^2_{|X[k]|} \tag{A.9}$$

where we need to know ${\sigma_{|X[k]|}}^2$.

Since $|X[k]| = \sqrt{(Re\{X[k]\})^2 + (Im\{X[k]\})^2}$, we can express $\sigma^2_{|A[k]|}$ in terms of $\sigma^2_{Re\{X[k]\}}$ and $\sigma^2_{Im\{X[k]\}}$ (Bevington and Robinson, 1992):

$$\sigma^2_{|A[k]|} = \frac{16}{N^2}\left(\sigma^2_{Re\{X[k]\}}\left(\frac{\partial|X[k]|}{\partial Re\{X[k]\}}\right)^2 + \sigma^2_{Im\{X[k]\}}\left(\frac{\partial|X[k]|}{\partial Im\{X[k]\}}\right)^2\right) \tag{A.10}$$

$$= \frac{16}{N^2}\frac{\sigma^2_{Re\{X[k]\}}(Re\{X[k]\})^2 + \sigma^2_{Im\{X[k]\}}(Im\{X[k]\})^2}{(Re\{X[k]\})^2 + (Im\{X[k]\})^2} \tag{A.11}$$

$$= \frac{16}{N^2}\left(\sigma^2_{Re\{X[k]\}}\cos^2(P[k]) + \sigma^2_{Im\{X[k]\}}\sin^2(P[k])\right) \tag{A.12}$$

$$\sigma_{|A[k]|} = \frac{4}{N}\sqrt{\sigma^2_{Re\{X[k]\}}\cos^2(P[k]) + \sigma^2_{Im\{X[k]\}}\sin^2(P[k])} \tag{A.13}$$

In order to compute the error in $|A[k]|$ we now need $\sigma^2_{Re\{X[k]\}}$ and $\sigma^2_{Im\{X[k]\}}$ which we can get from Equations A.2 and A.3 since we know the error in each phase of rotation ($\sigma^2_{x[n]}$):

$$\sigma^2_{Re\{X[k]\}} = \sum_{n=0}^{N-1} \sigma^2_{x[n]} \cos^2(\tfrac{2\pi}{N} kn) \tag{A.14}$$

$$\sigma^2_{Im\{X[k]\}} = \sum_{n=0}^{N-1} \sigma^2_{x[n]} \sin^2(\tfrac{2\pi}{N} kn) \tag{A.15}$$

The error in a peak-to-peak value can be computed from Equations A.13, A.14 and A.15 if the error in each phase of rotation ($\sigma^2_{x[n]}$) and the phase of the FFT ($P[k]$) are known.

Bibliography

Bevington, P. R. and Robinson, D. K. (1992). *Data Reduction and Error Analysis for the Physical Sciences.* WCB/McGraw-Hill, 2nd edition.

Brown, S. B., Arsdell, W. V., and Muhlstein, C. L. (1997). Materials reliability in MEMS devices. In *Transducers '97*, pages 591–593. 1997 International conference on Solid-State Sensors and Actuators, Chicago.

Davis, C. Q. (1994). *Estimation of Sub-Micrometer Translations of a Rigid Body Using Light Microscopy.* Master's thesis, Massachusetts Institute of Technology, Cambridge, MA.

Davis, C. Q. and Freeman, D. M. (1998a). Statistics of subpixel registration algorithms based on spatio-temporal gradients or block matching. *Optical Engineering*, 37(4):1290–1298.

Davis, C. Q. and Freeman, D. M. (1998b). Using a light microscope to measure motions with nanometer accuracy. *Optical Engineering*, 37(4):1299–1304.

Foley, J., van Dam, A., Feiner, S. K., and Hughes, J. F. (1990). *Computer Graphics: Principles and Practice.* Addison-Wesley, 2nd edition.

Freeman, D. M., Aranyosi, A. J., Gordon, M. J., and Hong, S. S. (1998). Multidimensional motion analysis of MEMS using computer microvision. In *Solid-State Sensor and Actuator Workshop*, pages 150–155. Transducer Research Foundation, Inc.

Freeman, D. M. and Davis, C. Q. (1996). Using video microscopy to characterize micromechanics of biological and manmade micromachines. In *Solid-State Sensor and Actuator Workshop*, pages 161–167. Transducer Research Foundation, Inc.

Horn, B. K. P. (1986). *Robot Vision.* MIT Press, Cambridge, MA.

Horn, B. K. P. and Weldon, Jr., E. (1988). Direct methods for recovering motion. *Internatl. J. of Computer Vision*, 2:51–76.

Inoué, S. (1986). *Video Microscopy.* Plenum Press, New York, NY.

Johnson, L. K. (1997). *Using Computer Microvision to Characterize the Motions of a Microfabricated Gyroscope.* Master's thesis, Massachusetts Institute of Technology, Cambridge, MA.

Karu, Z. Z. (1997). *Fast subpixel registration of 3-D images.* PhD thesis, Massachusetts Institute of Technology, Cambridge, MA.

Senturia, S. D. and Schmidt, M. A. (1997). Design and fabrication of microelectromechanical devices. Class notes, Course 6.971 (now 6.777), Massachusetts Intstitute of Technology, Cambridge, MA.